Towards a Correlation between Structural, Magnetic, and Luminescence Properties of CeF$_3$:Tb^{3+} Nanocrystals

Cristina Bartha, Corina Secu, Elena Matei, Catalin Negrila, Aurel Leca and Mihail Secu *

National Institute for Materials Physics, 077125 Magurele, Romania; cristina.bartha@infim.ro (C.B.);
cesecu@infim.ro (C.S.); elena.matei@infim.ro (E.M.); cnegrila@infim.ro (C.N.); lec.aurel@gmail.com (A.L.)

* Correspondence: msecu@infim.ro

Abstract: In this study, we report on the structural, magnetic, and optical properties of Tb^{3+}-doped CeF$_3$ nanocrystals prepared via a polyol-assisted route, followed by calcination. X-ray diffraction analysis and electron microscopy investigations have shown the formation of a dominant Ce$_{0.75}$F$_3$ nanocrystalline phase (of about 99%), with a relatively uniform distribution of nanocrystals about 15 nm in size. Magnetization curves showed typical paramagnetic properties related to the presence of Ce^{3+} and Tb^{3+} ions. The magnetic susceptibility showed a weak inflexion at about 150 K, assigned to the cerium ions' crystal field splitting. Under UV light excitation of the Ce^{3+} ions, we observed Tb^{3+} green luminescence with a quantum yield of about 20%.

Keywords: fluorides; nanocrystals; structure; magnetism; photoluminescence

1. Introduction

Rare-earth-doped nanofluorides are of great interest due to their high potential for application in various fields, e.g., lighting and displays, optical amplifiers, lasers, up-converters, and scintillators ([1–3] and references therein). Nanomaterials showing both luminescence and magnetic characteristics in particular are useful for a wide range of applications, such as multifunctional imaging and simultaneous diagnosis and therapy [4,5].

Among different inorganic fluorides, CeF$_3$ is one of the most versatile due to its wide range of bulk properties, such as high thermal and chemical stability, high density and resistance to radiation, fast response time, low vibrational energies, etc., and chemical flexibility of the structure allowing high solubility of rare-earth dopant ions. Another major advantage of this compound is related to the large spectrum of possible preparation methods, allowing for its processing in various sizes and morphologies, down to the nanometer scale. The bulk CeF$_3$ crystal has a hexagonal phase structure: a space group of $P3c1$ (D_{3d} ^{4}) with lattice constants a = 0.713 nm and c = 0.729 nm [5]. It exhibits efficient UV absorption due to the allowed electric dipole 4f→5d transition of Ce^{3+} ions and energy transfer to other rare-earth activators, which is useful for white LED phosphor applications [6–8]. In particular, various synthesis methods have been proposed for Tb^{3+}-doped CeF$_3$ nanocrystals, and the photoluminescence properties and energy transfer mechanism have been extensively investigated [9–12]. A less-studied aspect is related to the magnetic properties, which are strongly correlated with its electronic structure, whereas for the rare-earth dopant ions, these are related to the unpaired electrons in the inner 4f sub-shell. Investigations of the magnetic behavior of CeF$_3$ crystals are relatively limited and have been described within several models: crystal field theory [13], mixed-valent Ce^{3+}-Ce^{4+} behavior [14], or super-exchange interaction of cerium ions [15]. Recent investigations of CeF$_3$ nanodisks have revealed an anomalous behavior of the magnetic susceptibility at T $\cong$ 50 K, assigned to the processing-related defects and/or size effects [13–16].

The synthesis route may influence nanocrystals' structure through synthesis-induced defects, but to date, there has been little focus on the structural refinement analysis, and the mixed valency behavior of the cerium ions has been overlooked [17]. These aspects are crucial to understanding the interaction mechanisms relevant for both optical and magnetic properties, and their improvement for possible applications. In addition, the high ratio of ions at the surface (with unsaturated coordination), and the periodicity loss on the surface, result in structural modifications and defects that may affect all the properties, and therefore, knowledge of the nanocrystals' surface properties is highly relevant. The absolute novelty of this study derives from two aspects: (i) the complex structural analysis of terbium-doped cerium fluoride nanocrystals and its correlation with the influence of the material processing method, and (ii) the investigation of the specific magnetic behavior of the nanocrystals.

Herein, we report on the structural, magnetic, and optical properties of Tb^{3+}-doped CeF_3 nanocrystals prepared via a polyol assisted route. X-ray diffraction and electron microscopy techniques have been used for the structural and morphological characterization of the nanocrystals, whereas photoelectron spectroscopy was employed for the nanocrystals' surface analysis. Magnetic and optical properties (e.g., photoluminescence, quantum yield) have been presented and discussed.

2. Materials and Methods

2.1. Samples Preparation

For the preparation of Tb (8 mol%)-doped CeF_3 nanocrystalline powders, we used the chemical precipitation technique at room temperature mediated by the ethylene glycol solvent, similar to [18]. The raw materials $Ce(NO_3)_3 \cdot 6H_2O$ (99.5%), $Tb(NO_3)_3 \cdot xH_2O$ (99.9%), NH_4F (99.99%), and anhydrous ethylene glycol (99.8%) were used for the synthesis. Initially, a first solution was prepared by dissolving 0.102 g of NH_4F into 10 mL of ethylene glycol. Then, 0.3261 g $Ce(NO_3)_3 \cdot 6H_2O$ (99.5%) and 0.0358 g $Tb(NO_3)_3 \cdot xH_2O$ (99.9%) were dissolved into 5 mL of ethylene glycol. This second solution was slowly dropped into the first one, and the mixture was stirred for 1 min at room temperature until a transparent colloidal solution had formed. At the end, the nanoparticles were isolated by centrifugation of the colloidal solution, washed to remove the remaining reagent, and dried at 80 °C in air. Further annealing of the CeF_3:Tb powder was performed in open atmosphere for 1 h at 400 °C.

2.2. Samples Characterization

For the X-ray diffraction (XRD) measurements, we used a BRUKER D8 ADVANCE (Billerica, Massachusetts, USA), type X-ray diffractometer. The XRD pattern was recorded in the 20 to 60° range with 0.05° step and 3 s integration time. For the phase composition analysis and crystal structure refinement, we used the Rietveld method and a dedicated software (MAUD) [19,20], and starting parameters from PDF 04-005-7362 ($Ce_{0.75}F_3$) and PDF 00-008-6551 ($CeO_{1.66}$) files from the ICDD Powder Diffraction Files database [21]. The morphology of the samples was studied using a Zeiss MERLIN (Jena, Germany) Compact scanning electron microscope (SEM) with a GEMINI column, whereas for the chemical composition analysis, we used an EVO 50 XVP microscope from Zeiss equipped with an energy dispersive X-ray system (EDX) Quanta Bruker 200. For the magnetic properties' characterization, we used a superconducting quantum interference device (SQUID), and we measured the sample magnetization dependence on both magnetic fields up to 3 T, and on temperatures ranging from 5 to 300 K. A powder sample (17 mg) of CeF_3:Tb^{3+} was measured using a standard capsule, and its magnetic contribution (about 4%) was subtracted from the total magnetic signal. The temperature dependence of the magnetic susceptibility was measured under magnetic fields of 0.1 and 5 T applied perpendicularly to the sample. For the XPS measurements, we used a multianalysis SPECS system dedicated to surface analysis, equipped with a non-monochromatic source that provides a uniform X-Ray flux on the sample surface. The electron analyzer was a PHOIBOS150, with a 150 mm radius and a multichanneltron detector operating in large area mode and very low angular acceptance of 5° around the normal. The spectra of C1s, O1s, Ce3d, F1s, Tb3d, and Tb4d lines were recorded using a

Pass Energy of 10 eV, while the extended spectrum was recorded using a Pass Energy of 50 eV. For the spectra fitting and analysis, we used the Spectral Data Processor v.2.3 software (XPS International, Marlborough, Massachusetts, USA) and Voigt functions. In order to minimize the contamination, the XPS spectra were recorded on freshly calcinated samples after having been stored for 24 h in the high vacuum chamber. For the photoluminescence (PL) spectra, we used a FluoroMax 4P spectrophotometer (HORIBA Jobin Yvon, Kyoto, Japan); the spectra were corrected for the spectral sensitivity of the experimental set-up. The chromaticity analysis and quantum yield characterization were performed using the Quanta-Phy accessory of the spectrophotometer".

3. Results and Discussion

3.1. Structural and Morphological Characterisation

The XRD pattern of the CeF$_3$:Tb nanocrystalline powder calcinated at 400 °C is depicted in Figure 1; the results of the Rietveld analysis are presented in Figure 1 and Tables 1 and 2. The analysis showed the presence of a dominant Ce$_{0.75}$F$_3$ crystalline phase (of about 98.7%), accompanied by a much smaller CeO$_{1.66}$ crystalline fraction (of about 1.2%), both stable at room temperature. The formation of Ce$_{0.75}$F$_3$ as a dominant crystalline phase is the consequence of the synthesis and processing conditions that result in a material with defects and multiple fraction valencies of cerium ions [17]. The lattice parameters are very close to those from the ICDD database (Table 1), and the nanocrystallite's size agrees very well with SEM microscopy data (see below).
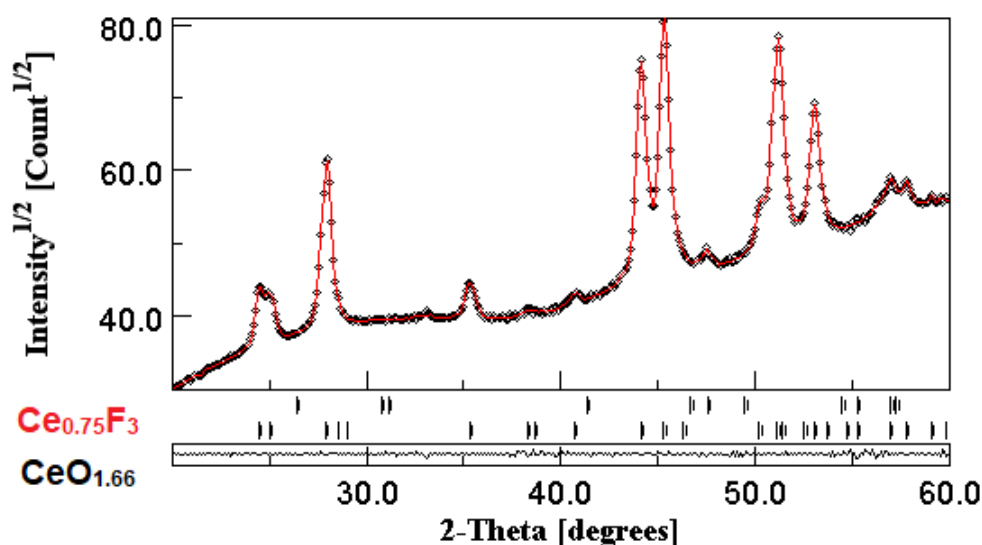
Figure 1. XRD pattern (black curve) and Rietveld refinement plot (red curve) of CeF$_3$:Tb nanocrystalline powder calcinated at 400 °C, with the Bragg reflections for Ce$_{0.75}$F$_3$ and CeO$_{1.66}$ crystalline phases indicated by vertical bars; the lower trace represents the difference curve between observed and calculated patterns.

From Table 2, it can be observed that the positions of the Ce^{3+} ions and their first neighbor (F$_1$ ions) are slightly shifted compared to the reference. As the Tb^{3+} ions ionic radius (R = 1.095A) is smaller than that of Ce^{3+} ions (R = 1.196A), a substitutional incorporation is very likely; the photoluminescence spectra showed a crystal-field structure of the Tb^{3+} luminescence bands (see below). However, the XRD pattern analysis has shown small changes in the cell parameters (Table 1), and therefore, a partial interstitial incorporation of Tb^{3+} ions cannot be completely rejected. The microstrain values for both phases indicated different values of the distances between the crystallographic planes, which can be related to the lattice defects produced during the synthesis and lattice distortion induced by the Tb^{3+} ions' incorporation into the Ce$_{0.75}$F$_3$ crystalline lattice.

Table 1. Rietveld refinement results for Tb^{3+} doped CeF_3 nanocrystalline powders calcinated at 400 °C.

Crystalline Phase	Cerium Fluoride ($Ce_{0.75}F_3$)	Cerium Oxide ($CeO_{1.66}$)	R Factors (%)
Weight fraction (%)	98.798 ± 0.001	1.2017 ± 0.002	
Crystal size (nm)		13.985(2)	
Crystal system	Hexagonal	Cubic	
Space group	P-3c1	Fm-3m	R_{wp} (%) = 2.994
Calculated Unit Cell (Å)	a = b = 7.1053(3) c = 7.2614(1)	a = 5.415(1)(2)	R_B (%) = 2.358 $R_{exp.}$ = 1.015
Cell_angle_alpha	90°	90°	χ^2 = 2.049
Cell_angle_beta	90°	90°	
Cell_angle_gamma	120°	90°	
Unit Cell according PDF (Å) (ref. [21])	a = b = 7.1 c = 7.27	a = b = 5.4112(10)	
Cell Volume (Å^3)	317.38 (3)	158.45(1)	
Microstrain	1.7×10^{-5} ± 0.002	2.3×10^{-6} ± 0.001	

Table 2. Atomic site occupancy for Tb^{3+} doped CeF_3 nanocrystalline powders.

Atoms	$Ce_{0.75}F_3$ (calc.)	$Ce_{0.75}F_3$ (theor.)	$Ce_{0.75}F_3$ (calc.)	$Ce_{0.75}F_3$ (theor.)	$Ce_{0.75}F_3$ (calc.)	$Ce_{0.75}F_3$ (theor.)	Wyckoff Site	Atom Site Occupancy (theor/calc)
	x		**y**		**z**			
F_1	0.3862(3)	0.356	0.3610(4)	0.328	0.0712(3)	0.096	12g	1/0.8393(5)
Ce	0.3394(5)	0.3333	0	0	0.2504(1)	0.25	6f	0.75/0.7503(2)
F_3	0.3334(2)	0.3333	0.6671(5)	0.6666	0.2267(3)	0.167	4d	1/0.9851(5)
F_4	0	0	0	0	0.2497(2)	0.25	2a	1/0.9877(4)

The SEM image analysis has shown a distribution of round-shaped nanoparticles of about 15 nm in size (Figures 2 and 3). Chemical composition analysis resulting from the EDX spectra (Figure 3) has shown a relative agreement (within the experimental errors) between the atoms' concentrations in the precursor chemicals and in the annealed samples: 14 at%(Ce), 79 at%(F), 1.5 at%(O), and 1.5 at%(Tb).
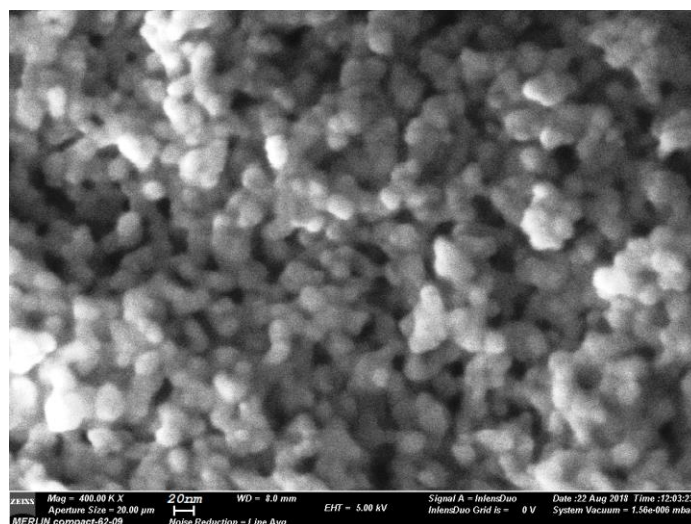
Figure 2. SEM image of CeF_3:Tb nanocrystalline powder calcinated at 400 °C.

It can be seen that the F to Ce ratio (of about 5.5) is relatively close to the four expected for $Ce_{0.75}F_3$ phase (Table 1), but higher than the three expected for CeF_3, indicating Ce^{3+} ion deficiency and lower Tb^{3+} ion concentration than expected; XRD analysis has shown $Ce_{0.75}F_3$ phase, i.e., Ce^{3+} ion deficiency. We suppose that the reason is related to the NH_4F amount used for the synthesis, since it plays a critical role in controlling the final morphology and size of the product [11]. In the present case, for the stoichiometric NH_4F amount generally used, we obtained spherical nanoparticles about 15 nm in size (Figure 2) with Ce^{3+} ion deficiency as resulting from the EDX and XRD analyses (Table 1 and Figure 3), this aspect having been overlooked by previous studies. The Ce^{3+} ion deficiency suggested that a higher NH_4F amount is required to accomplish the reaction and the Tb^{3+}-doping process. However,

for higher NH_4F content, different nanocrystals morphologies were obtained with hundreds of nm in size, accompanied by crystallinity and luminescence signal improvement [11]. Therefore, by using a stoichiometric NH_4F amount, we obtained nanocrystals "with defects", i.e., a $Ce_{0.75}F_3$ nanocrystalline phase with lower "effective" Tb^{3+} ions' dopant concentration.
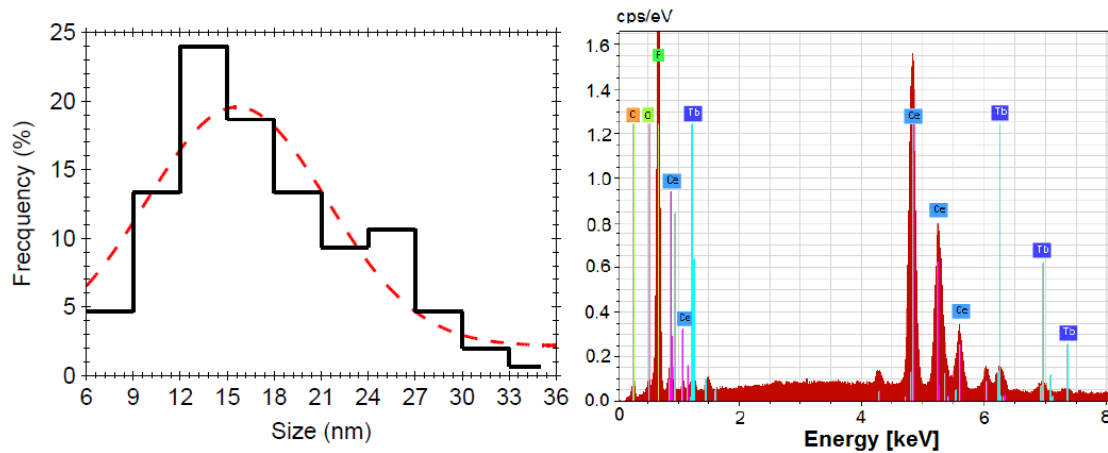

Figure 3. Nanocrystals size distribution (**left**) and the corresponding energy dispersive X-ray (EDX) analysis with the characteristic X-ray lines assignment (**right**); the dotted curve is just a guide for the eyes.

3.2. X-ray Photoelectron Spectroscopy (XPS) Characterization

For the investigation of the nanocrystals' surface, we used the XPS technique, which is recognized as a valuable investigation tool for the chemistry associated to different bonds and related compounds ([22] and references therein).

Figure 4 shows different spectral lines of the XPS spectrum of CeF_3:Tb nanocrystalline powder annealed at 400 °C. The region between 880 and 925 eV was assigned to the Ce3d line of the Ce^{3+} ion species, and the energies indicate Ce-F bonds [23]. The XPS spectrum is composed of several convoluted peaks that correspond to the Ce $3d^{5/2}$ and $3d^{3/2}$ lines, and each of them is split into two lines due to the multiplet splitting effect arising from the two possible states after photoionization: $4f^1$ and $4f^2$. The 884.57 and 902.97 eV peaks were due to the $4f^2$ final state, whereas the others at 888.12 and 906.38 eV were due to the $4f^1$ final state. The 899.05 and 918.11 eV peaks were assigned to the "loss" type peaks due to the energy transfer from the F2p orbitals to the conduction band orbitals of Ce (4d,5d,6s) [24,25]. The CeF_3 nanocrystalline phase was revealed by the strong single F1s peak at 685.20 eV, in connection to the Ce 3d peaks. The oxygen species' characteristic peaks are observable in the energy region at around 530–532 eV. The 529.07 eV peak was assigned to the oxidized metal, whereas the 531.99 eV peak was assigned to the adsorbed species and carbon bonds; low signal of the oxygen indicates low oxygen concentration. The oxidized metal species were observed in LaF_3 nanoparticles within a nanometric layer at their surfaces [18] and are related to the calcination process. Regarding the Tb^{3+}-ion dopant, its characteristic spectrum in the 4d region between 140 and 160 eV showed a complex multiplet splitting (not presented), which is difficult to analyze. However, the values of the energy bonds and the spectrum shape attribute the observed features to Tb^{3+} ion species. In the 3d region, the $Tb3d^{3/2}$ peak overlaps with the $Ce3p^{1/2}$ peak, and the two 1241.96 and 1245.19 eV energy peaks were assigned to the $Tb3d^{5/2}$ multiplet splitting, corresponding to the $3d^9 4f^9$ and $3d^{10} 4f^8$ final states. As the bond energies are slightly higher than for corresponding metal or oxides [26,27], and fluorine electronegativity is higher than for oxides, the peaks were assigned to the Tb-F bonds, due to the Tb^{3+} incorporation in the CeF_3 matrix.
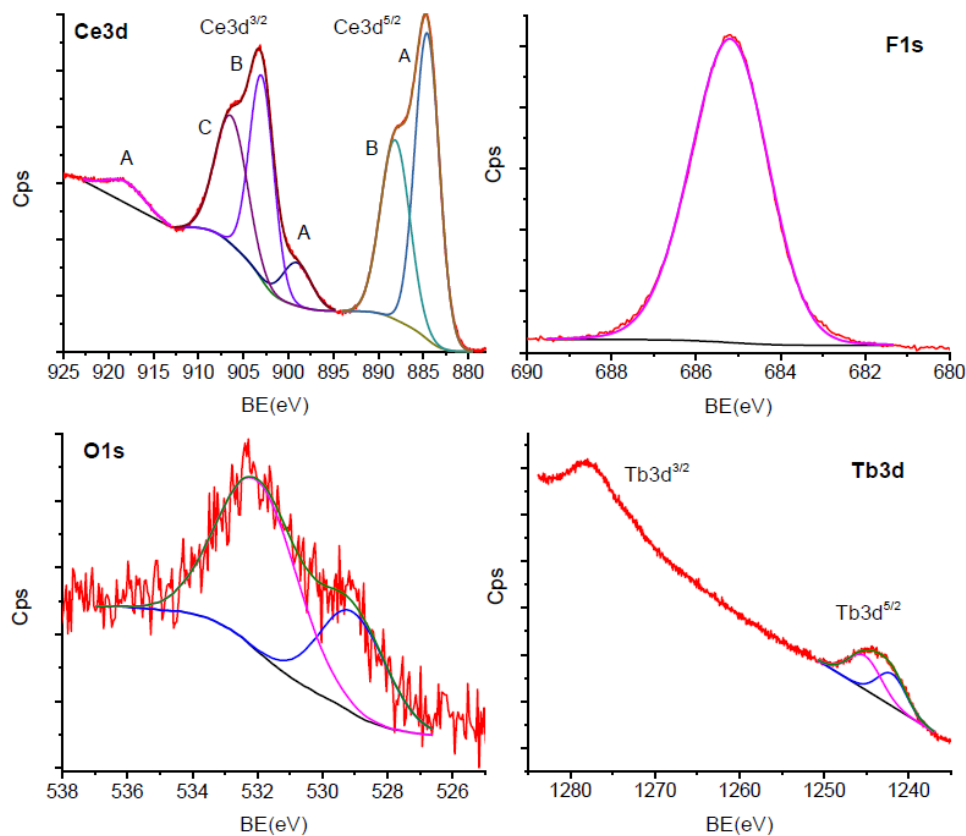
Figure 4. The XPS spectrum of the CeF$_3$:Tb nanocrystalline powder calcinated at 400 °C.

3.3. Magnetic Properties

The paramagnetic properties of the CeF$_3$:Tb^{3+} nanocrystalline powder calcinated at 400 °C are confirmed by the magnetization vs. magnetic field dependencies (at low and high temperatures) of the magnetization curves (Figure 5).
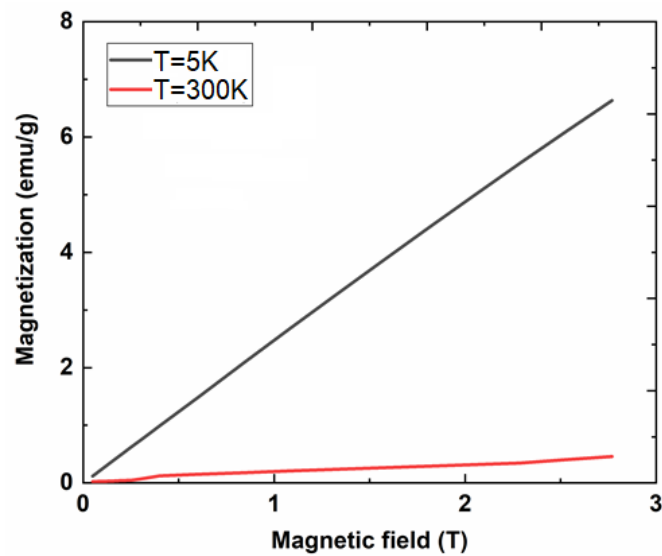
Figure 5. Magnetization vs. magnetic field dependence measured at T = 300 K and T = 5 K recorded on CeF$_3$:Tb nanocrystalline powder calcinated at 400 °C.

Temperature dependence of both magnetization and the inverse magnetic susceptibility (computed from the experimental data) are depicted in Figure 6. In both cases (for applied magnetic fields of 0.1 and 5 T), the magnetic susceptibility shows a typical paramagnetic behavior with small inflection at around 150 K that can be attributed to the Ce^{3+} ions' crystal field splitting. Tb^{3+} contribution is very weak considering the small percentage of Ce^{3+} substitution. It is known that cerium is a Kramer's ion, having an odd number of 4f electrons, and the maximum possible splitting of the $^2F_{5/2}$ state is in three doublets. When Ce^{3+} ions are placed in a hexagonal symmetry, the maximum splitting of levels will occur [28]. Energy splitting calculations showed that, for a hexagonal crystal field in cerium, the doublets were excited to 30 and 150 K above the ground state [29]. These values are comparable to those reported at 89 and 206 K for Ce^{3+} ions in hexagonal yttrium [30].
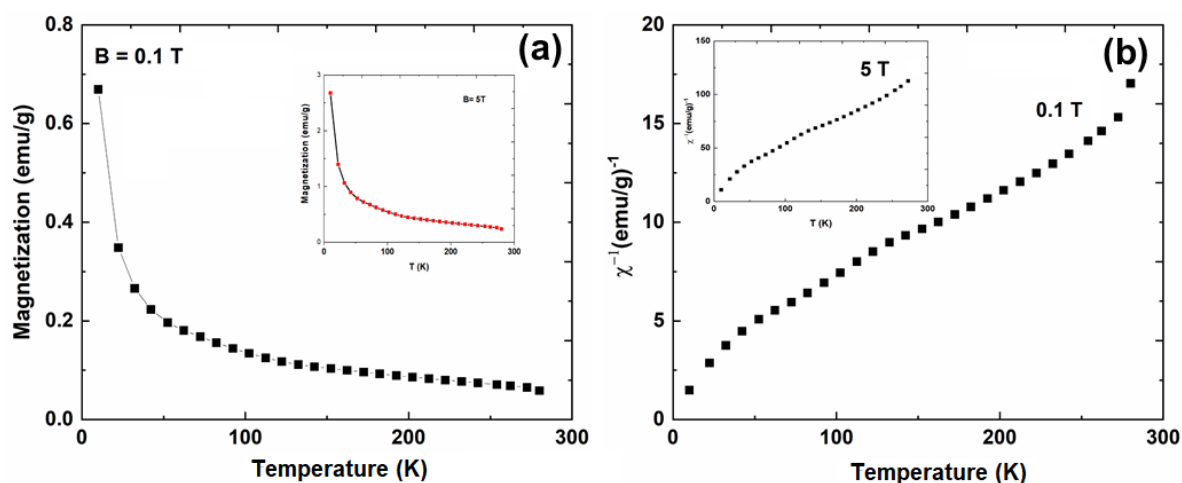

Figure 6. Temperature dependencies of the magnetization at an applied magnetic field of 5 T (inset) and 0.1 T, respectively, (**a**) and the inverse magnetic susceptibility at a perpendicularly applied magnetic field of 5 T (in inset) and 0.1 T, respectively (**b**).

3.4. Photoluminescence Properties

The photoluminescence properties and energy transfer mechanism for Tb^{3+}-doped CeF_3 have been extensively investigated in CeF_3 [9–12], and therefore, we do not address them in detail here. The energy levels of Tb^{3+} allow an efficient energy transfer (ET) from the 5d-4f emission of the Ce^{3+} ions, resulting in high light output (Figure 6—left). Under 250 nm UV light pumping, Ce^{3+} ions are excited from $^7F_{7/2,5/2}$ ground state levels to the 4f5d excited energy levels. Then, a radiative energy transfer to the Tb^{3+} excited levels occurs, followed by radiative deexcitation from the green emitting levels of Tb^{3+} ($^5D_4 \rightarrow ^7F_j$; J = 5, 4, 3)—Figure 6. The maximal ET rate is about 89% for 7.5 mol% Tb^{3+}-doping [5], or 79.7% for 10mol% Tb^{3+}-doping [10]. In the present case, we computed the ET efficiency (η_{ETE}) from Ce^{3+} to the Tb^{3+} activator ions using the Ce^{3+} luminescence signal intensities in the absence (I_0) and presence (I) of Tb^{3+}-activator ions [31]: "$\eta_{ETE} = 1 - I/I_0$", and we obtained an ET efficiency value of about 92%.

The luminescence and excitation spectra recorded on undoped and Tb-doped CeF_3 nanocrystalline powders calcinated at 400 °C are depicted in Figure 7. Under 250 nm UV light excitation, the undoped nanoparticles showed weak 375 nm luminescence assigned to the 5d-4f radiative deexcitation (Figure 7—dotted curve) [9]. This luminescence cannot be seen in the doped nanocrystal sample, where we observed only the Tb^{3+}-related luminescence peaks at 542, 585, and 620 nm ($^5D_4 \rightarrow ^7F_j$; J = 5, 4, 3). The PL bands showed a crystal field structure associated to Ce^{3+} substitution by the Tb^{3+} in the CeF_3 crystalline lattice. The excitation spectrum of the green 545 nm Tb^{3+}-luminescence showed the characteristic 4f-4f transitions of the Tb^{3+} ions, accompanied by a broad and intense peak at 250 nm assigned to the Ce^{3+} transitions $^7F_{7/2,5/2}$ to 4f5d excited states.
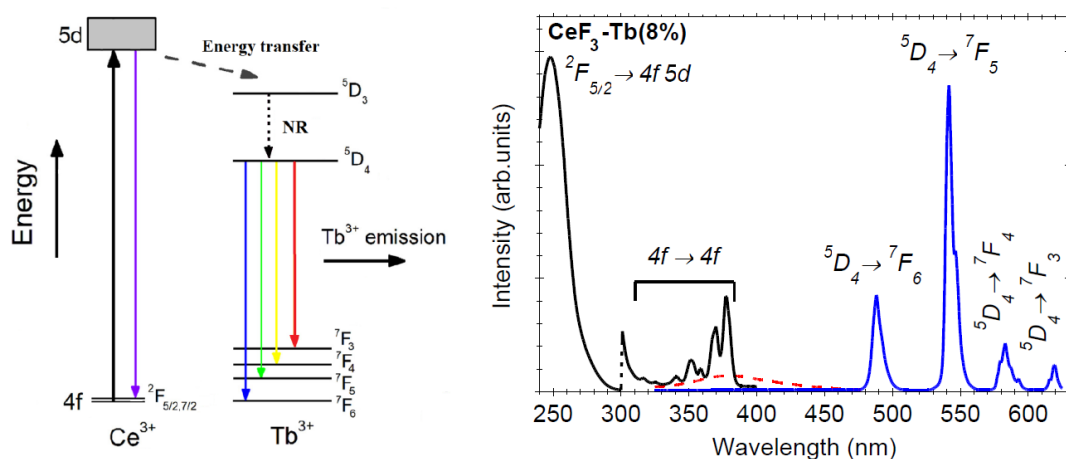
Figure 7. Energy level scheme of the Ce^{3+} and Tb^{3+} ions (**left**) and the photoluminescence excited at 250 nm with the excitation spectrum of the 545 nm luminescence recorded on CeF_3:Tb nanocrystalline powder calcinated at 400 °C (**right**); photoluminescence of undoped CeF_3 nanocrystalline sample is shown for comparison (dotted curve).

Figure 8 shows the Commission Internationale de l'Eclairage (CIE) chromaticity diagram of CeF_3:Tb^{3+} nanocrystalline powder with the coordinates x = 0.252 and y = 0.725 in the region of green light characteristic to the Tb^{3+} luminescence region. In the present case, the quantum yield (QY) of the Tb^{3+} ions green-related luminescence is about 20% (for 250 nm excitation wavelength) and is smaller than for YAG:Ce phosphor nanoparticles (of about 130 to 270 nm size), where a QY of 70–72% was reported [32]. On the other hand, the QY is influenced by the nanocrystals' size: the QY of $Ca_3Sc_2Si_3O_{12}$:Ce^{3+} nanopowders is about 50% and increases to 70–72% for microparticles [33].
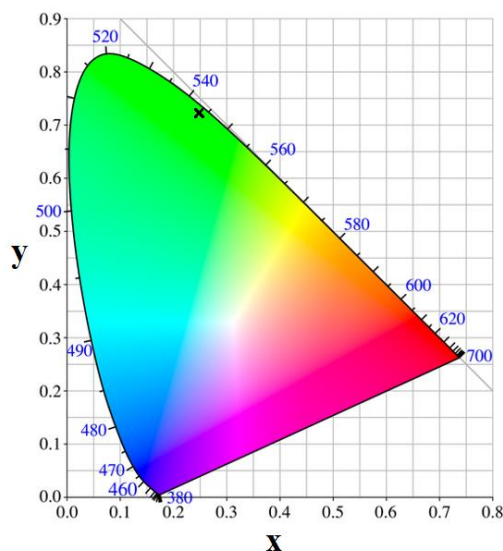
Figure 8. The chromaticity coordinates of the Commission Internationale de l'Eclairage (CIE) chromaticity diagram of CeF_3:Tb nanocrystalline powder calcinated at 400 °C.

4. Conclusions

In this study, Tb^{3+}-doped CeF_3 nanocrystals showing both magnetic and photoluminescence properties were prepared at room temperature via a polyol mediated route followed by calcination.

X-ray diffraction analysis has shown a dominant $Ce_{0.75}F_3$ nanocrystalline phase (of about 99%), in which Tb^{3+} ions are substitutionally and interstitially incorporated, accompanied by traces of $CeO_{1.66}$ (of about 1%). Electron microscopy investigations have shown a relatively uniform distribution of

nanocrystals about 15 nm in size. X-ray photoelectron spectroscopy has evidenced the presence of an oxidized metal layer at the nanocrystals' surface due to the calcination process. Magnetization curves showed typical paramagnetic properties related to the Ce^{3+} and Tb^{3+} ions. The magnetic susceptibility behavior for low and high applied magnetic fields (0.1 T and 5 T, respectively) highlighted a small inflection around 150 K, due to the crystal field splitting related to the cerium ions. Under UV light excitation, an efficient energy transfer from the Ce^{3+} to Tb^{3+} ions resulted in a strong Tb^{3+} green luminescence with a quantum yield of about 20%.

The combination of fluorescent alongside magnetism-integrated functions of multifunctional nanoparticles could lead to new opportunities in nano-bio related *applications*.

Author Contributions: The samples were prepared by C.S., and C.B., E.M., C.N., and M.S. cooperated carefully together on the physical characterization and analysis of the data: A.L. was involved specifically with magnetic measurements, C.B. with magnetic measurement analysis and structural analysis with XRD, E.M. with electron microscopy characterization by SEM, C.N. with X-ray spectroscopy, and C.S. and M.S. with photoluminescence and quantum yield characterization. The manuscript was written by M.S. in collaboration with C.B. and C.N. and approved by all authors. All authors contributed to discussions and reviewed the manuscript. All authors have read and agreed to the published version of the manuscript.

Conflicts of Interest: The authors declare no conflict of interest.

References

1. Escudero, A.; Becerro, A.I.; Carrillo-Carrion, C.; Núñez, N.O.; Zyuzin, M.V.; Laguna, M.; González, D.; Ocaña, M.; Parak, W.J. Rare earth based nanostructured materials: Synthesis, functionalization, properties and bioimaging and biosensing applications. *Nanophotonics* **2017**, *6*, 881–921. [CrossRef]

2. Sharma, R.K.; Mudring, A.V.; Ghosh, P. Recent trends in binary and ternary rare-earth fluoride nanophosphors: How structural and physical properties influence optical behavior. *J. Lumin.* **2017**, *189*, 44–63. [CrossRef]

3. Fedorov, P.; Luginina, A.A.; Kuznetsov, S.V.; Osiko, V.V. Nanofluorides. *J. Fluor. Chem.* **2011**, *132*, 1012–1039. [CrossRef]

4. Lee, G.H.; Chang, Y.; Kim, T.J. *Ultrasmall Lanthanide Oxide Nanoparticles for Biomedical Imaging and Therapy*; Woodhead Publishing Series in Biomaterial; Woodhead Publishing: Cambridge, MA, UK, 2004.

5. Cheetham, A.K.; Fender, B.E.F.; Fuess, H.; Wright, A.F. A powder neutron diffraction study of lanthanum and cerium trifluorides. *Acta Crystallogr.* **1976**, *B32*, 94–97. [CrossRef]

6. Samanta, T.; Sarkar, S.; Adusumalli, V.N.K.B.; Praveen, A.E.; Mahalingam, V. Enhanced visible and near infrared emissions via Ce^{3+} to Ln^{3+} energy transfer in Ln^{3+}-doped CeF_3 nanocrystals (Ln = Nd, Sm). *Dalton Trans.* **2016**, *45*, 78–84. [CrossRef]

7. Li, C.; Li, F.; Li, T.; Bai, T.; Wang, L.; Shi, Z.; Feng, S. A facile synthesis and photoluminescence properties of water-dispersible RE^{3+} doped CeF_3 nanocrystals and solid nanocomposites with polymers. *Dalton Trans.* **2012**, *41*, 4890–4895. [CrossRef]

8. Sayed, F.N.; Grover, V.; Dubey, K.A.; Sudarsan, V.; Tyagi, A.K. Solid state white light emitting systems based on CeF_3:RE^{3+} nanoparticles and their composites with polymers. *J. Colloid Interface Sci.* **2011**, *353*, 445–453. [CrossRef]

9. Li, X.; Zhang, W.; Dong, L.; Liu, D.; Qi, Z. Low temperature molten salt synthesis of CeF_3 and CeF_3:Tb^{3+} phosphors with efficient luminescence properties. *J. Lumin.* **2019**, *205*, 122–128. [CrossRef]

10. Sun, Z.; Li, Y.; Zhang, X.; Yao, M.; Ma, L.; Chen, W. Luminescence and energy transfer in water soluble CeF_3 and CeF_3:Tb^{3+} nanoparticles. *J. Nanosci. Nanotechnol.* **2009**, *9*, 6283–6291. [CrossRef]

11. Qu, X.; Yang, H.K.; Chung, J.W.; Moon, B.K.; Choi, B.C.; Jeong, J.H.; Kim, K.H. Polyol-mediated solvothermal synthesis and luminescence properties of CeF_3, and CeF_3:Tb^{3+} nanocrystals. *J. Solid State Chem.* **2011**, *184*, 246–251. [CrossRef]

12. Wang, Z.L.; Quan, Z.W.; Jia, P.Y.; Lin, C.K.; Luo, Y.; Chen, Y.; Fang, J.; Zhou, W.; O'Connor, C.J.; Lin, J. A facile synthesis and photoluminescent properties of redispersible CeF_3, CeF_3:Tb^{3+} and CeF_3:Tb^{3+}/LaF_3 (core/shell) nanoparticles. *Chem. Mater.* **2006**, *18*, 2030–2037. [CrossRef]

13. Savinkov, A.V.; Korableva, S.L.; Tagirov, M.S.; Suzuki, H.; Matsumoto, K.; Abe, S. Revised measurements and interpretation of magnetic properties of oriented CeF$_3$ single crystals. *J. Low Temp. Phys.* **2016**, *185*, 603–608. [CrossRef]

14. Xu, Y.; Duan, M. Theory of Faraday rotation and susceptibility of rare-earth trifluorides. *Phys. Rev. B* **1992**, *46*, 11636–11641. [CrossRef] [PubMed]

15. Gong-Qiang, L.; Wen-Kang, Z.; Xing, Z. Quantitative analyses of magnetic and magneto-optical properties in cerium trifluoride. *Phys. Rev. B* **1993**, *48*, 16091–16094. [CrossRef] [PubMed]

16. Chaput, F.; Lerouge, F.; Bulin, A.L.; Amans, D.; Odziomek, M.; Faure, A.-C.; Monteil, M.; Dozov, I.; Parola, S.; Bouquet, F.; et al. Liquid-crystalline suspensions of photosensitive paramagnetic CeF^3 nanodiscs. *Langmuir* **2019**, *35*, 16256–16265. [CrossRef] [PubMed]

17. Shoko, E.; Smith, M.F.; McKenzie, R.H. Mixed valency in cerium oxide crystallographic phases: Determination of valence of the different cerium sites by the bond valence method. *Phys. Rev. B* **2009**, *79*, 134108. [CrossRef]

18. Secu, C.E.; Matei, E.; Negrila, C.; Secu, M. The influence of the nanocrystals size and surface on the Yb/Er doped LaF$_3$ luminescence properties. *J. Alloy. Compd.* **2019**, *791*, 1098–1104. [CrossRef]

19. Rietveld, H.M. A profile refinement method for nuclear and magnetic structures. *J. Appl. Crystallogr.* **1969**, *2*, 65–71. [CrossRef]

20. Lutterotti, L.; Matthies, S.; Wenk, H.-R. MAUD (material analysis using diffraction): A user friendly Java program for Rietveld texture analysis and more. In Proceedings of the Twelfth International Conference on Textures of Materials (ICOTOM-12), Montreal, Canada, 9–13 August 1999.

21. PDF-ICDD. *Powder Diffraction File (PDF-4+ 2018 Software 4.18.0.2)*; International Centre for Diffraction Data, 12 Campus Boulevard: Newtown Square, PA, USA, 2011.

22. Baer, D.R.; Engelhard, M.; Johnson, G.E.; Laskin, J.; Lai, J.; Mueller, K.; Munusamy, P.; Thevuthasan, S.; Wang, H.-F.; Washton, N.; et al. Surface characterization of nanomaterials and nanoparticles: Important needs and challenging opportunities. *J. Vac. Sci. Technol. A Vac. Surf. Films* **2013**, *31*, 050820. [CrossRef]

23. Barreca, D.; Gasparotto, A.; Maccato, C.; Maragno, C.; Tondello, E. Cerium (III) Fluoride Thin Films by XPS. *Surf. Sci. Spectra* **2006**, *13*, 87. [CrossRef]

24. Kalkowski, G.; Kaindl, G.; Wortman, G.; Lentz, D.; Krause, S. 4f-ligand hybridization in CeF$_4$ and TbF$_4$ probed by core-level spectroscopies. *Phys. Rev. B* **1988**, *37*, 1376–1382. [CrossRef] [PubMed]

25. Bossche, J.V.D.; Neyts, K.; De Visschere, P.; Corlatan, D.; Pauwels, H.; Vercaemst, R.; Fiermans, L.; Poelman, D.; Van Meirhaeghe, R.L.; Laflére, W.H.; et al. XPS Study of TbF, and TbOF Centres in ZnS. *Phys. Stat. Sol. (A)* **1994**, *146*, K67. [CrossRef]

26. Lee, C.J.; Vashishtha, S.; Sayal, A.; Weaver, J.F. Oxidation of a c-Tb$_2$O$_3$(111) thin film by the sequential formation of stoichiometric phases. *Surf. Sci.* **2020**, *694*, 121555. [CrossRef]

27. Sarma, D.D.; Rao, C.N.R. XPES studies of oxides of second-and third-row transition metals including rare earths. *J. Electron Spectrosc. Relat. Phenom.* **1980**, *20*, 25–45. [CrossRef]

28. Segal, E.; Wallace, W. Rare earth ions in a hexagonal field III. *J. Solid State Chem.* **1974**, *6*, 203–213. [CrossRef]

29. Bleaney, B. *Rare Earth Research II: Proceedings of the Third Conference on Rare Earth Research*; Vorres, K., Ed.; Gordon and Breach: New York, NY, USA, 1964; p. 417.

30. Yoshida, S.; Sugawara, T. Kondo effect in single crystals of Y-Ce alloys. *Phys. Lett. A* **1969**, *30*, 422–423. [CrossRef]

31. Bourcet, J.C.; Fong, F.K. Quantum efficiency of diffusion limited energy transfer in La$_{1-x-y}$Ce$_x$Tb$_y$PO$_4$. *J. Chem. Phys.* **1974**, *60*, 34–39. [CrossRef]

32. Borlaf, M.; Kubrin, R.; Aseev, V.; Petrov, A.Y.; Nikonorov, N.; Graule, T. Deep submicrometer YAG:Ce phosphor particles with high photoluminescent quantum yield prepared by flame spray synthesis. *J. Am. Ceram. Soc.* **2017**, *100*, 3784–3793. [CrossRef]

33. Batentschuk, M.; Brabec, C.J.; Khaidukov, N.; Levchuk, I.; Osvet, A.; Römling, L.; Schröppel, F. , Van Deun, R.; Zorenko, Y. Highly Luminescent Ca$_3$Sc$_2$Si$_3$O$_{12}$:Ce^{3+} Silicate Garnet Nano- and Microparticles with 50–70% Photoluminescence Quantum Yields as Efficient Phosphor Converters for White LEDs. *TechConnect Briefs* **2017**, *4*, 194–197.